RESEARCH ARTICLE

[1]School of Physics, Huazhong University of Science and Technology, Wuhan 430074, China; [2]International Joint Laboratory on Quantum Sensing and Quantum Metrology, Huazhong University of Science and Technology, Wuhan 430074, China; [3]Institut für Quantenoptik & IQST, Albert-Einstein Allee 11, Universität Ulm, D-89081 Ulm, Germany; [4]Institut für Theoretische Physik & IQST, Albert-Einstein Allee 11, Universität Ulm, D-89081 Ulm, Germany; [5]Interdisciplinary Theoretical and Mathematical Sciences Program (iTHEMS), RIKEN, Wako, Saitama 351-0198, Japan and [6]Center for Nonlinear Phenomena and Complex Systems, Université Libre de Bruxelles, B-1050 Brussels, Belgium

PHYSICS

Experimental measurement of the quantum geometric tensor using coupled qubits in diamond

Min Yu[1,2,†], Pengcheng Yang[1,2,†], Musang Gong[1,2], Qingyun Cao[3,1,2], Qiuyu Lu[1,2], Haibin Liu[1,2], Shaoliang Zhang[1,2,*], Martin B. Plenio[4,2], Fedor Jelezko[3,2], Tomoki Ozawa[5], Nathan Goldman[6,*] and Jianming Cai[1,2,*]

ABSTRACT

Geometry and topology are fundamental concepts, which underlie a wide range of fascinating physical phenomena such as topological states of matter and topological defects. In quantum mechanics, the geometry of quantum states is fully captured by the quantum geometric tensor. Using a qubit formed by an NV center in diamond, we perform the first experimental measurement of the complete quantum geometric tensor. Our approach builds on a strong connection between coherent Rabi oscillations upon parametric modulations and the quantum geometry of the underlying states. We then apply our method to a system of two interacting qubits, by exploiting the coupling between the NV center spin and a neighboring ^{13}C nuclear spin. Our results establish coherent dynamical responses as a versatile probe for quantum geometry, and they pave the way for the detection of novel topological phenomena in solid state.

Keywords: quantum geometry, topological physics, quantum measurement, quantum control, quantum information

*Corresponding authors. E-mails: ngoldman@ulb.ac.be; shaoliang@hust.edu.cn; jianmingcai@hust.edu.cn
†Equally contributed to this work.

INTRODUCTION

The quantum geometric tensor (QGT) constitutes a central and ubiquitous concept in quantum mechanics, by providing a geometric structure to the Hilbert space [1–5]. The imaginary part of this tensor corresponds to the well-known Berry curvature [6,7], which acts as an effective 'electromagnetic' tensor in parameter space. This geometric quantity, which is formally associated with the parallel transport of wave functions [8], is responsible for striking observable phenomena such as the geometric phase [8], the anomalous Hall effect [9] and topological states of matter [10]. In contrast, the real part of the QGT constitutes the Fubini-Study metric [2,3,5], which defines a notion of distance (a Riemannian metric) in parameter space through the overlap of wavefunctions. This 'quantum metric', which is intimately related to quantum fluctuations and dissipative responses of the system [2,5,11,12], has been shown to play an important role in various contexts, including quantum phase transitions [13], open quantum systems [14], orbital magnetism [15,16], localization in insulators [11], semi-classical dynamics [17,18], excitonic Lamb-shifts in transition-metal dichalcogenides [19], superfluidity in flat bands [20] and topological matter [21,22]. In the context of quantum information, the quantum metric is equivalent to the quantum Fisher information, which is a witness for multipartite entanglement [23].

Various manifestations of the QGT have been observed in experiments, using very different physical platforms and probes. On the one hand, the local Berry curvature has been detected in ultra-cold atomic gases [24–26], coupled optical fibers [27], and solids [28,29]. On the other hand, a first manifestation of the quantum metric—the so-called Wannier-spread functional of Bloch bands [30]—was recently measured in cold atoms [31], based on the proposal [32]; see [12,33–35] for other proposals to detect quantum geometry. Nevertheless, direct and systematic measurement of the complete QGT has never been performed.

Here, we report on the first experimental measurement of the complete QGT, using a qubit formed by an NV center spin in diamond. Following

the proposal of [32], we exploit the relation between the QGT and the response of quantum systems upon parametric modulations to map out the full Fubini-Study metric as well as the local Berry curvature of the underlying quantum states. We then apply our method to a system of two interacting qubits, obtained by coupling the NV center spin to a nearby ^{13}C nuclear spin. Our results not only enforce the deep connections between out-of-equilibrium dynamics and quantum geometry [36–44], but also reveal a universal tool for detection of geometric and topological properties in quantum systems.

DETECTING THE QGT THROUGH RABI OSCILLATION

We start by considering the Hamiltonian $H(\lambda)$ of a generic discrete quantum system, which depends on a set of dimensionless parameters $\lambda = (\lambda_1, \lambda_2, \cdots, \lambda_N)$, where N is the dimension of parameter space. For a single qubit, the relevant parameter space corresponds to the two-dimensional Bloch sphere. Defining the eigenstates and eigenvalues of this generic Hamiltonian, $H(\lambda)|n(\lambda)\rangle = \epsilon_n(\lambda)|n(\lambda)\rangle$, a geometric structure emerges upon projecting the dynamics onto a single (non-degenerate) band $\epsilon_n(\lambda)$. The resulting quantum geometry is captured by the QGT, which is defined as [7]

$$\chi_{\mu\nu}^{(n)} = \langle \partial_\mu n(\lambda) | (1 - |n(\lambda)\rangle\langle n(\lambda)|) | \partial_\nu n(\lambda) \rangle. \tag{1}$$

For simplicity, hereafter we denote $\partial_\mu \equiv \partial_{\lambda_\mu}$. The real part $Re(\chi_{\mu\nu}) = g_{\mu\nu}$ is the Fubini-Study metric, which introduces a notion of distance in parameter space, while the imaginary part $Im(\chi_{\mu\nu}) = -F_{\mu\nu}/2$ is related to the Berry curvature $F_{\mu\nu}$ responsible for the Berry phase. It is useful to express the QGT in the form

$$\chi_{\mu\nu}^{(n)} = \sum_{m \neq n}$$
$$\times \frac{\langle n(\lambda) | \partial_\mu H(\lambda) | m(\lambda) \rangle \langle m(\lambda) | \partial_\nu H(\lambda) | n(\lambda) \rangle}{(\epsilon_m(\lambda) - \epsilon_n(\lambda))^2}, \tag{2}$$

so as to highlight the relation between this geometric quantity and the coupling matrix elements connecting the eigenstates $|n(\lambda)\rangle$ and $|m(\lambda)\rangle$ upon a parametric modulation [32],

$$\Omega_{n \leftrightarrow m}(\lambda) \propto \langle m(\lambda) | \partial_\mu H(\lambda) | n(\lambda) \rangle. \tag{3}$$

EXPERIMENTAL SETUP

In our experiment, we first perform a full quantum-geometric measurement using a two-level system, as described by the general Hamiltonian

$$H(\theta, \varphi) = \frac{A}{2} \begin{pmatrix} \cos\theta & \sin\theta e^{-i\varphi} \\ \sin\theta e^{i\varphi} & -\cos\theta \end{pmatrix}, \tag{4}$$

where the angles (θ, φ) form the relevant parameter space (the Bloch sphere). Considering the low-energy dressed state, the components of the QGT read $g_{\theta\theta} = \frac{1}{4}$, $g_{\varphi\varphi} = \frac{1}{4}\sin^2\theta$, $g_{\theta\varphi} = 0$, $F_{\theta\varphi} = \sin\theta/2$. These components fully characterize the underlying quantum geometry: the quantum metric g corresponds to the natural metric of a sphere S^2, embedded in R^3 with fixed radius $R = \frac{1}{2}$, while the Berry curvature $F_{\theta\varphi}$ corresponds to the 'magnetic' field of a fictitious Dirac monopole located at the center of that sphere [22].

The experimental setup is sketched in Fig. 1D. The two-level system in Eq. (4) is obtained from a single nitrogen-vacancy (NV) center in an electronic grade diamond. We apply a magnetic field $B_z = 509\,G$ along the NV axis to lift the degeneracy of the states $m_s = \pm 1$. A two-level system is supported by the spin sublevels $m_s = 0$ and $m_s = -1$. We first prepare the system in the eigenstate of the Hamiltonian $H(\theta_0, \varphi_0)$, i.e. $n(\theta_0, \varphi_0)\rangle = \cos\frac{\theta_0}{2} | -1\rangle + \sin\frac{\theta_0}{2}e^{i\varphi_0}|0\rangle$. This is achieved by first applying a 532 nm green laser pulse to initialize the NV center spin in the $m_s = 0$ state. A subsequent microwave pulse $H_i(t) = \Omega \sin(\omega_0 t + \varphi_0)\sigma_x$, applied over a duration $t_{\theta_0} = \frac{\theta_0}{\Omega}$, rotates the NV center spin around the axis $\hat{n}(\varphi_0) = (\cos\varphi_0, \sin\varphi_0, 0)$ by an angle θ_0. The initial state preparation is verified by a spin-locking type experiment, which confirms that the NV spin is prepared in the eigenstate of $H(\theta_0, \varphi_0)$ [see supplementary data].

The precise control over the AWG allows us to engineer the microwave driving field with accurate amplitude and phase modulation. This leads to implementation of the generic two-level system

$$H(t) = \frac{\omega_0}{2}\sigma_z + V(t)\sigma_x, \tag{5}$$

where $V(t) = (A\sin\theta_t)\cos[\omega_0 t - f(t) + \varphi_t]$. In the experiment, we calibrate the driving amplitude in the Hamiltonian [Eq. (5)] with the output power of the AWG by measuring the Rabi frequency of the NV center spin [see supplementary data]. The amplitude modulation $A\sin\theta_t$ and the phase modulation $-f(t) + \varphi_t$ are synthesized by waveform programming in the AWG. The additional phase control function has the form $f(t) = A\int_0^t \cos\theta_\tau d\tau \cong A\cos\theta_0 J_0(a_\theta)t - (4A\sin\theta_0/\omega) J_1(a_\theta)\sin^2(\omega t/2)$, where $J_{0,1}$ are the zeroth and
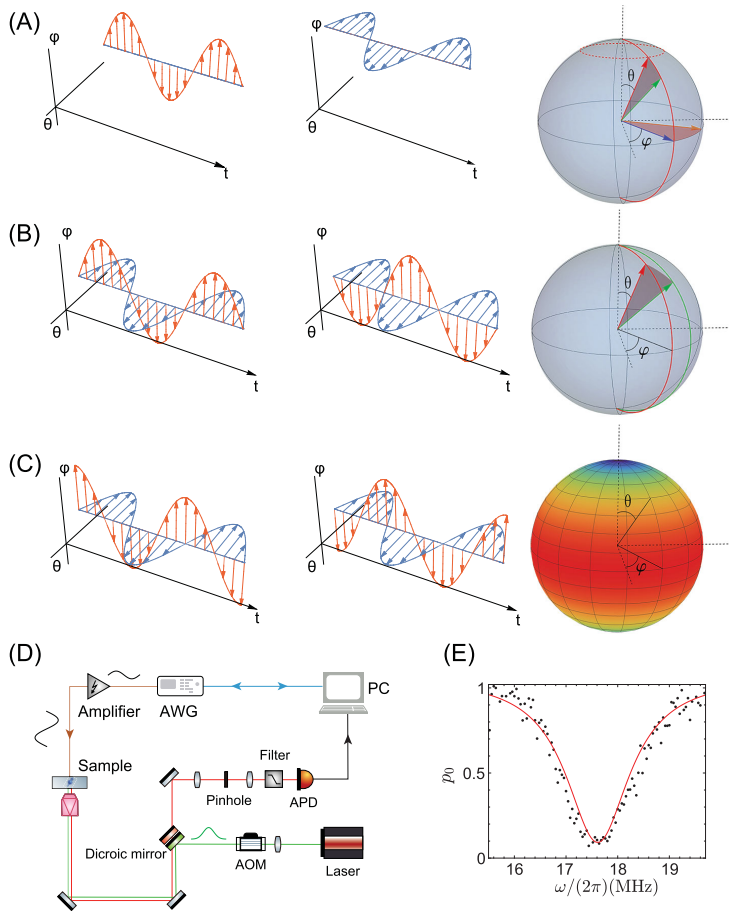
Figure 1. Probing quantum geometry through coherent responses on parametric modulations. (A–C) show different types of parametric modulations (θ_t, φ_t), including (A, B) linear parametric modulation $\theta_t = \theta_0 + a_\theta \sin(\omega t)$, $\varphi_t = \varphi_0 + a_\varphi \sin(\omega t)$ for measurement of the diagonal [off-diagonal] element of the Fubini-Study metric with $a_\theta = 0$ or $a_\varphi = 0$ (A) [$a_\theta = \pm a_\varphi \neq 0$ (B)]; (C) elliptical parametric modulation for the measurement of the local Berry curvature (as indicated by color map) with $\theta_t = \theta_0 + a_\theta \sin(\omega t)$ and $\varphi_t = \varphi_0 \pm a_\varphi \cos(\omega t)$. (D) Experimental setup used for the quantum-geometric measurement, based on an NV center spin in diamond. A green laser pulse polarizes the NV center spin into the $|m_s = 0\rangle$ state. The engineered microwave created from an arbitrary waveform generator (Tektronix AWG 70002A, 16GS/s) is amplified before being delivered to the sample and coherently drives the NV center spin. The NV center spin state is detected by an APD via spin-dependent fluorescence. (E) An example of parametric-modulation resonance measurement. The probability that the NV center spin remains in the initial eigenstate at time $T = 400$ ns as a function of the modulation frequency, for a linear parametric modulation $\theta_t = \theta_0 + a_\theta \sin(\omega t)$, $\varphi_t = \varphi_0$ with $(\theta_0, \varphi_0) = (\frac{5\pi}{6}, 0)$ and $a_\theta = 0.1$.

first order Bessel functions of the first kind, respectively [see supplementary data]. Taking the limit $\omega_0 \gg A$, such an engineered microwave driving field allows us to realize the effective Hamiltonian in Eq. (4) with the designed parametric modulation [see supplementary data]:

$$H_{eff}(t) \cong \frac{A}{2}$$
$$\times \left[\cos\theta_t\sigma_z + \sin\theta_t\left(\cos\varphi_t\sigma_x + \sin\varphi_t\sigma_y\right)\right].$$
(6)

The parametric modulation drives a coherent transition between the eigenstates of $H(\theta_0, \varphi_0)$, which is detected by rotating the NV center spin around the axis $\hat{n}(\varphi_0)$ by an angle $2\pi - \theta_0$. This rotation maps the eigenstates of $H(\theta_0, \varphi_0)$ back to the NV center spin state $|0\rangle$ and $|-1\rangle$, which is then measured by spin-dependent fluorescence.

EXPERIMENTAL RESULTS

In the experiment, we implement two types of modulations [32]: (a) a 'linear' modulation $\theta_t = \theta_0 + a_\theta \sin(\omega t)$, $\varphi_t = \varphi_0 + a_\varphi \sin(\omega t)$; (b) an 'elliptical' modulation $\theta_t = \theta_0 + a_\theta \sin(\omega t)$, $\varphi_t = \varphi_0 + a_\varphi \cos(\omega t)$; see Fig. 1A–C. Setting a_θ, $a_\varphi \ll 1$, the time-dependent Hamiltonian can be expressed as

$$H(\theta_t, \varphi_t) \cong H(\theta_0, \varphi_0) + a_\theta(\partial_\theta H)\sin(\omega t)$$
$$+ a_\varphi(\partial_\varphi H)\sin(\omega t) : linear$$
$$+ a_\varphi(\partial_\varphi H)\cos(\omega t) : elliptical.$$
(7)

After preparing the NV center spin in the eigenstate $|n(\theta_0, \varphi_0)\rangle$ of the Hamiltonian $H(\theta_0, \varphi_0)$, we apply the engineered microwave driving field with parametric modulation [see Eq. (5)] and fix the time duration T. We sweep the parametric modulation frequency ω, and measure the probability $p_0(T)$ that the NV spin remains in the initial eigenstate $|n(\theta_0, \varphi_0)\rangle$. In Fig. 1E, we show an example of such a parametric-modulation resonance measurement; see supplementary data for the experimental data using other types of modulations. The results indicate that a coherent transition between the eigenstates becomes resonant when $\omega \cong A \equiv \omega_c$. We then measure the resonant coherent oscillation upon parametric modulation with $\omega = \omega_c$, as shown in Fig. 2A–C. The observed Rabi frequencies under resonant parametric modulations, which reveal the information about the coupling matrix elements connecting the eigenstates [see Eq. (3)] upon parametric modulation, are shown in Fig. 2D–F. The experimental results allow us to determine the quantum geometry of the prepared dressed states precisely.

As a central result, we show in Fig. 3 the experimental extraction of the full QGT, based on Rabi-oscillation measurements. This provides a first demonstration that coherent responses upon parametric modulations can be used as a powerful tool to access the complete geometry of a discrete quantum system. We point out that the present quantum-geometry measurement is based on coherent dynamic responses upon periodic driving, and in this sense, it does not rely on any adiabaticity constraints (i.e. small modulation velocity [36,37]). It should be noted, however, that this method uses small modulation amplitudes, and hence small
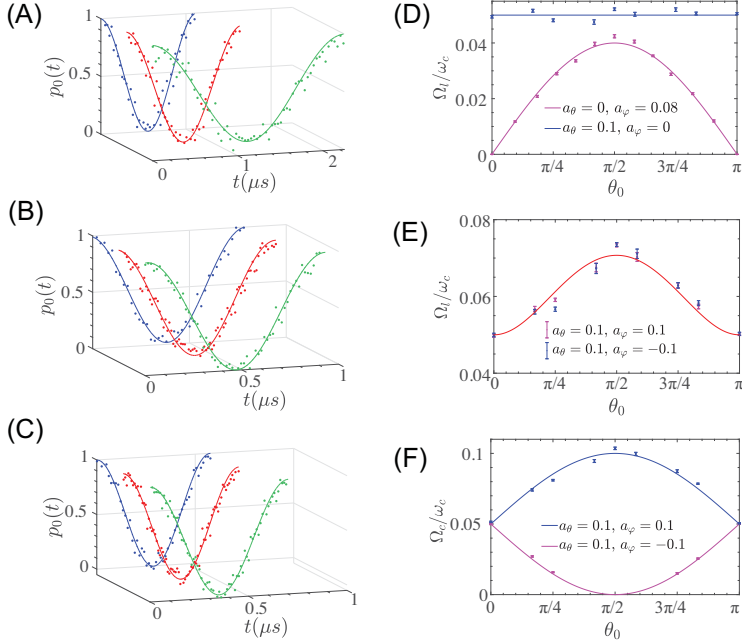
Figure 2. Coherent transitions induced by parametric modulations. (A, B) Resonant oscillation under a linear parametric modulation with $a_\theta = 0$, $a_\varphi = 0.08$ (A) and $a_\theta = 0.1$, $a_\varphi = 0.1$ (B). (C) Resonant oscillation under an elliptical parametric modulation with $a_\theta = 0.1$, $a_\varphi = 0.1$. The other experimental parameters are: (A) $\omega_c = (2\pi)20.98$ MHz ($\theta_0 = \frac{\pi}{6}$, green), $(2\pi)21.61$ MHz ($\theta_0 = \frac{\pi}{3}$, red), $(2\pi)20.73$ MHz ($\theta_0 = \frac{\pi}{2}$, blue); (B) $\omega_c = (2\pi)19.11$ MHz ($\theta_0 = \frac{\pi}{6}$, green), $(2\pi)17.8$ MHz ($\theta_0 = \frac{5\pi}{12}$, red), $(2\pi)16.72$ MHz ($\theta_0 = \frac{\pi}{2}$, blue); (C) $\omega_c = (2\pi)19.11$ MHz ($\theta_0 = \frac{\pi}{6}$, green), $(2\pi)17.8$ MHz ($\theta_0 = \frac{5\pi}{12}$, red), $(2\pi)16.72$ MHz ($\theta_0 = \frac{\pi}{2}$, blue). (D–F) Rabi frequency of resonant coherent transitions upon parametric modulations (in the unit of resonant frequency ω_c), as a function of the parameter θ_0, for linear (D, E) and elliptical (F) parametric modulations. The curves show theoretical predictions. In (A–F), we set the parameter $\varphi_0 = 0$.
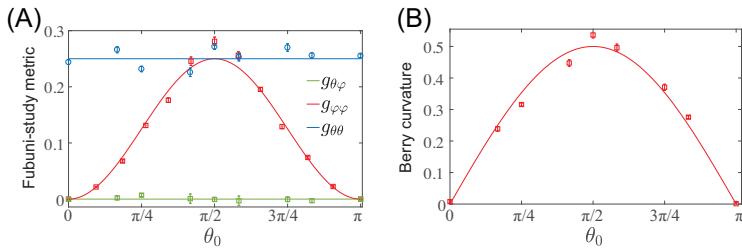
Figure 3. Extraction of the complete quantum geometric tensor. (A) The measured Fubini-Study metric, compared with the theoretical predictions $g_{\theta\varphi} = 0$ (green curve), $g_{\varphi\varphi} = \sin^2\theta_0/4$ (red curve) and $g_{\theta\theta} = 1/4$ (blue curve). (B) The measured local Berry curvature $F_{\theta\varphi}$ is compared with the theoretical prediction $F_{\theta\varphi} = \sin\theta_0/2$. The experimental parameters are the same as in Fig. 2.

Rabi frequencies, which require systems exhibiting long coherence times. The agreement between the experiment results and the theoretical predictions can be improved by increasing the measurement time, which allows for better determination of the oscillation frequency. Furthermore, in contrast with the excitation-rate measurement of [31,32,41], the QGT is extracted from Rabi oscillations [39], where

the initial state is recovered after each Rabi period; in principle, this allows for detection of geometry and topology through a non-destructive measurement.

Besides, our quantum-geometry measurement can also be used to characterize the topology of the underlying system. For this analysis, we extend the Hamiltonian to the form

$$H(\theta, \varphi) = \frac{A}{2}\begin{pmatrix} \cos\theta + r & \sin\theta e^{-i\varphi} \\ \sin\theta e^{i\varphi} & -\cos\theta - r \end{pmatrix}, \tag{8}$$

where r is a tunable parameter. As for Eq. (4), the geometry of the Hamiltonian in Eq. (8) is that of a fictitious monopole located close to a sphere S^2, whose position in parametric space depends on the additional parameter r. The topology of the system then relies on whether this fictitious monopole is located inside the sphere or not, as captured by the Chern number $C = \frac{1}{2\pi}\int_{S^2} F_{\theta\varphi}d\theta d\varphi$ [13]. Figure 4 shows the Berry curvature measurement in two distinct topological phases. In the non-trivial regime, the Chern number can equally be determined from the metric $C = \frac{1}{2\pi}\int_{S^2}(2\sqrt{\bar{g}})d\theta d\varphi = \frac{1}{2\pi}\int_{S^2}|F_{\theta\varphi}|d\theta d\varphi$, where $\bar{g} = g_{\theta\theta}g_{\varphi\varphi} - (g_{\theta\varphi})^2$ is the determinant of the QGT [22]. Altogether, these results indicate that topology can indeed be finely analyzed based on our geometric-detection scheme.

APPLICATION TO INTERACTING QUBITS

As a second application, we further extend our experiment to extract the QGT of an interacting two-qubit system. The interacting two-qubit system is formed by an NV center electron spin coupled to a ^{13}C nuclear spin located in the vicinity of the NV center. We determine the strength of the corresponding spin-spin interactions using a pulsed optically detected magnetic resonance experiment; we obtain the interaction parameters: $A_x \approx 2.79$ MHz and $A_z \approx 11.832$ MHz [see Eq. (9) below]. By engineering microwave driving fields with designed frequency and phase, we obtain the following effective Hamiltonian

$$\begin{aligned} H_{rot}(\theta, \varphi) = &\frac{\Omega_{mw}}{2} \\ &\times \left[\cos\theta\sigma_z + \sin\theta\left(\cos\varphi\sigma_x + \sin\varphi\sigma_y\right)\right] \\ &+ \left(\frac{\gamma_n B_\parallel}{2} - \frac{A_z}{4}\right)\tau_z - \frac{A_x}{4}\tau_x \\ &- \frac{A_z}{4}\sigma_z \otimes \tau_z - \frac{A_x}{4}\sigma_z \otimes \tau_x, \end{aligned} \tag{9}$$

where σ and τ are Pauli operators associated with the first and second qubits, respectively. Henceforth, we denote the eigenstates of the Hamiltonian in
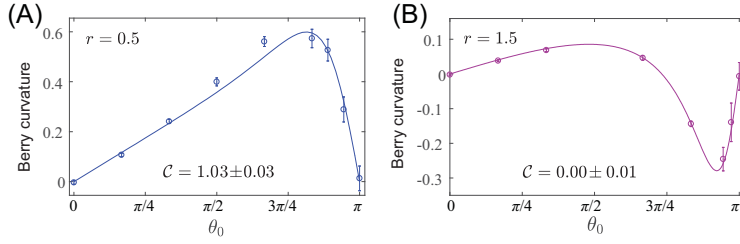
Figure 4. Berry curvature measurement across the topological transition. (A, B) show the measured local Berry curvature $F_{\theta\varphi}$ for the Hamiltonian in Eq. (8), which describes a Dirac monopole located inside (A, $r = 0.5$) and outside (B, $r = 1.5$) the Bloch sphere. The curves represent the corresponding theoretical values. The Chern number extracted from the data is indicated in both panels.
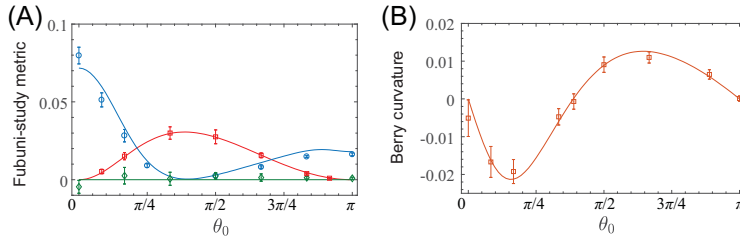
Figure 5. Quantum geometry of an interacting two-qubit system. (A) The measured Fubini-Study metric, compared with the theoretical predictions: $g_{\theta\varphi}$ (green curve), $g_{\varphi\varphi}$ (red curve) and $g_{\theta\theta}$ (blue curve). (B) The measured local Berry curvature $F_{\theta\varphi}$ is compared with the theoretical prediction (curve). The amplitude of the driving field [see Eq. (9)] is $\Omega_{mw} = 2.13$ MHz. The Chern number estimated from the integral of the Berry curvature is C = 0.00 ± 0.01, which is in agreement with the prediction (C = 0) in this strongly interacting regime.

Eq. (9) as $|\Psi_1\rangle$, $|\Psi_2\rangle$, $|\Psi_3\rangle$, $|\Psi_4\rangle$, according to their ordered eigenenergies $\epsilon_1 < \epsilon_2 < \epsilon_3 < \epsilon_4$.

The competition between the local term (Ω_{mw}) and the spin-spin interaction in the Hamiltonian Eq. (9) leads to a rich topological phase diagram. In the regime $\Omega_{mw} \gg \Omega_{mw}^{(c_1)}$, where

$$\Omega_{mw}^{(c_1)} = \frac{1}{2}\left[-\gamma_n B_\| + \sqrt{\left(\gamma_n B_\| - A_z\right)^2 + A_x^2}\right], \tag{10}$$

the spin-spin interaction becomes less significant and we thus recover the topological properties of the two-level system, for which the Chern number is C = 1 in the eigenstate $|\Psi_3\rangle$ (see the measurements described in the previous section); note that the other eigenstates exhibit similar behaviors. The spin-spin interaction eventually dominates upon decreasing the value of the local parameter; below the critical value, $\Omega_{mw} < \Omega_{mw}^{(c_1)}$, the Chern number of the eigenstate changes from C = 1 to C = 0, which can be seen as a drastic effect of the spin-spin interaction. This vanishing of the Chern number in the strongly interacting regime is clearly captured by our QGT measurement, as reported in Fig. 5. These results demonstrate the measurement of both the Fubini-Study metric and the Berry curvature deep

in the interacting regime, and show excellent agreement with theoretical predictions [see supplementary data].

As previously noted, the QGT contains information regarding the entanglement properties of interacting systems, through the concept of quantum Fisher information [23]. As an interesting perspective, our detection method could be applied to more complex interacting systems in view of revealing their quantum fluctuations and entanglement properties.

CONCLUSION

To summarize, we have experimentally demonstrated a powerful connection between the quantum geometric tensor and the coherent dynamic response of a quantum system upon a parametric drive. Based on this fundamental relation, we first extracted the complete QGT, including all the components of the Fubini-Study metric and those of the local Berry curvature, by driving Rabi oscillations in a single qubit. These measurements clearly revealed the topological (monopole-type) structure associated with this simple setting. We point out that this method is readily applicable to observe other intriguing topological defects, such as tensor monopoles defined in 4D parameter spaces [22]. Furthermore, we have applied this detection method to an interacting two-qubit system, which suggests potential applications to many-body quantum systems with geometric features [12,32,45]. Altogether, our results demonstrate that coherent dynamic responses can serve as a powerful tool to access the geometric and topological properties of quantum systems and open a way to explore the fundamental role of the QGT in various scenarios, ranging from many-body systems to open quantum systems.

NOTE ADDED

Materials and methods are available as supplementary material. Two other experimental measurements of the QGT were reported after the completion of our work [46], in polaritons [47] and superconducting qubits [48].

SUPPLEMENTARY DATA

Supplementary data are available at *NSR* online.

ACKNOWLEDGEMENTS

REFERENCES

1. Kibble TWB. Geometrization of quantum mechanics. *Commun Math Phys* 1979; **65**: 189–201.

2. Provost J and Vallee G. Riemannian structure on manifolds of quantum states. *Commun Math Phys* 1980; **76**: 289–301.

3. Anandan J and Aharonov Y. Geometry of quantum evolution. *Phys Rev Lett* 1990; **65**: 1697–700.

4. Brody DC and Hughston LP. Geometric quantum mechanics. *J Geom Phys* 2001; **38**: 19–53.

5. Kolodrubetz M, Sels D and Mehta P *et al.* Geometry and non-adiabatic response in quantum and classical systems. *Phys Rep* 2017; **697**: 1–87.

6. Simon B. Holonomy, the quantum adiabatic theorem, and Berry's phase. *Phys Rev Lett* 1983; **51**: 2167–70.

7. Berry MV. Quantal phase factors accompanying adiabatic changes. *Proc R Soc London Ser A* 1984; **392**: 45–57.

8. Bohm A, Mostafazadeh A and Koizumi H *et al. The Geometric Phase in Quantum Systems: Foundations, Mathematical Concepts, and Applications in Molecular and Condensed Matter Physics.* New York: Springer-Verlag Berlin Heidelberg, 2003.

9. Nagaosa N, Sinova J and Onoda S *et al.* Anomalous Hall effect. *Rev Mod Phys* 2010; **82**: 1539–92.

10. Hasan MZ and Kane CL. Colloquium: topological insulators. *Rev Mod Phys* 2010; **82**: 3045–67.

11. Souza I, Wilkens T and Martin RM. Polarization and localization in insulators: generating function approach. *Phys Rev B* 2000; **62**: 1666–83.

12. Ozawa T and Goldman N. Probing localization and quantum geometry by spectroscopy. *Phys Rev Res* 2019; **1**: 032019(R).

13. Zanardi P, Giorda P and Cozzini M. Information-theoretic differential geometry of quantum phase transitions. *Phys Rev Lett* 2007; **99**: 100603.

14. Albert VV, Bradlyn B and Fraas M *et al.* Geometry and response of Lindbladians. *Phys Rev X* 2016; **6**: 041031.

15. Gao Y, Yang SA and Niu Q. Geometrical effects in orbital magnetic susceptibility. *Phys Rev B* 2015; **91**: 214405.

16. Piéchon F, Raoux A and Fuchs J-N *et al.* Geometric orbital susceptibility: quantum metric without Berry curvature. *Phys Rev B* 2016; **94**: 134423.

17. Bleu O, Malpuech G and Gao Y *et al.* Effective theory of nonadiabatic quantum evolution based on the quantum geometric tensor. *Phys Rev Lett* 2018; **121**: 020401.

18. Lapa MF and Hughes TL. Semiclassical wave packet dynamics in nonuniform electric fields. *Phys Rev B* 2019; **99**: 121111(R).

19. Srivastava A and Imamoğlu A. Signatures of Bloch-band geometry on excitons: nonhydrogenic spectra in transition-metal Dichalcogenides. *Phys Rev Lett* 2015; **115**: 166802.

20. Julku A, Peotta S and Vanhala TI *et al.* Geometric origin of superfluidity in the Lieb-Lattice flat band. *Phys Rev Lett* 2016; **117**: 045303.

21. Roy R. Band geometry of fractional topological insulators. *Phys Rev B* 2014; **90**: 165139.

22. Palumbo G and Goldman N. Revealing tensor monopoles through quantum-metric measurements. *Phys Rev Lett* 2018; **121**: 170401.

23. Hauke P, Heyl M and Tagliacozzo L *et al.* Measuring multipartite entanglement through dynamic susceptibilities. *Nat Phys* 2016; **12**: 778–82.

24. Li T, Duca L and Reitter M *et al.* Bloch state tomography using Wilson lines. *Science* 2016; **352**: 1094–7.

25. Duca L, Li T and Reitter M *et al.* An Aharonov-Bohm interferometer for determining Bloch band topology. *Science* 2015; **347**: 288–92.

26. Fläschner N, Rem BS and Tarnowski M *et al.* Experimental reconstruction of the Berry curvature in a Floquet Bloch band. *Science* 2016; **352**: 1091–4.

27. Wimmer M, Price HM and Carusotto I *et al.* Experimental measurement of the Berry curvature from anomalous transport. *Nat Phys* 2017; **13**: 545–50.

28. Banks HB, Wu Q and Valovcin DC *et al.* Dynamical Birefringence: electron-hole recollisions as probes of Berry curvature. *Phys Rev X* 2017; **7**: 041042.

29. Luu TT and Wörner HJ. Measurement of the Berry curvature of solids using high-harmonic spectroscopy. *Nat Commun* 2018; **9**: 916.

30. Marzari N and Vanderbilt D. Maximally localized generalized Wannier functions for composite energy bands. *Phys Rev B* 1997; **56**: 12847–65.

31. Asteria L, Tran DT and Ozawa T *et al.* Measuring quantized circular dichroism in ultracold topological matter. *Nat Phys* 2019; **15**: 449–54.

32. Ozawa T and Goldman N. Extracting the quantum metric tensor through periodic driving. *Phys Rev B* 2018; **97**: 201117(R).

33. Neupert T, Chamon C and Mudry C. Measuring the quantum geometry of Bloch bands with current noise. *Phys Rev B* 2013; **87**: 245103.

34. Kolodrubetz M, Gritsev V and Polkovnikov A. Classifying and measuring geometry of a quantum ground state manifold. *Phys Rev B* 2013; **88**: 064304.

35. Bleu O, Solnyshkov DD and Malpuech G. Measuring the quantum geometric tensor in two-dimensional photonic and exciton-polariton systems. *Phys Rev B* 2018; **97**: 195422.

36. Roushan P, Neill C and Chen Y *et al.* Observation of topological transitions in interacting quantum circuits. *Nature* 2014; **515**: 241–4.

37. Gritsev V and Polkovnikov A. Dynamical quantum Hall effect in the parameter space. *Proc Natl Acad Sci USA* 2012; **109**: 6457–62.

38. Schroer MD, Kolodrubetz MH and Kindel WF *et al.* Measuring a topological transition in an artificial spin-1/2 system. *Phys Rev Lett* 2014; **113**: 050402.

39. Tran DT, Cooper NR and Goldman N. Quantized Rabi oscillations and circular dichroism in quantum Hall systems. *Phys Rev A* 2018; **97**: 061602(R).

40. de Juan F, Grushin AG and Morimoto T *et al.* Quantized circular photogalvanic effect in Weyl semimetals. *Nat Commun* 2017; **8**: 15995.

41. Tran DT, Dauphin A and Grushin AG *et al.* Probing topology by 'heating': quantized circular dichroism in ultracold atoms. *Sci Adv* 2017; **3**: e1701207.

42. Wang C, Zhang P and Chen X *et al.* Scheme to measure the topological number of a Chern insulator from quench dynamics. *Phys Rev Lett* 2017; **118**: 185701.

43. Fläschner N, Vogel D and Tarnowski M *et al.* Observation of dynamical vortices after quenches in a system with topology. *Nat Phys* 2018; **14**: 265–8.

44. Tarnowski M, Ünal FN and Fläschner N *et al.* Measuring topology from dynamics by obtaining the Chern number from a linking number. *Nat Commun* 2019; **10**: 1728.

45. Repellin C and Goldman N. Detecting fractional Chern insulators through circular dichroism. *Phys Rev Lett* 2019; **122**: 166801.

46. Yu M, Yang P and Gong M *et al.* Experimental measurement of the complete quantum geometry of a solid-state spin system. arXiv: 1811.12840.

47. Gianfrate A, Bleu O and Dominici L *et al.* Measurement of the quantum geometric tensor and of the anomalous Hall drift. *Nature* 2020; **578**: 381–5.

48. Tan X, Zhang D-W and Yang Z *et al.* Experimental measurement of the quantum metric tensor and related topological phase transition with a superconducting qubit. *Phys Rev Lett* 2019; **122**: 210401.